The Magnetic Free Energy in Active Regions

Final Report for NASA grant NAG-5-7438

Principle Investigator:

Dr. Thomas R. Metcalf
Lockheed Martin Solar and Astrophysics Lab., Orgn. L9-41, B-252
3251 Hanover St.
Palo Alto, CA 94304

Co-Investigator:

Dr. Donald L. Mickey / Dr. Barry J. LaBonte
University of Hawaii, Institute for Astronomy
2680 Woodlawn Dr.
Honolulu, HI 96822

2001 September 15

Contents

1 Introduction

The magnetic field permeating the solar atmosphere governs much of the structure, morphology, brightness and dynamics observed on the Sun. The magnetic field, especially in active regions, is thought to provide the power for energetic events in the solar corona, such as solar flares and Coronal Mass Ejections (CME) and is believed to energize the hot coronal plasma seen in EUV or X-rays. The question remains what specific aspect of the magnetic flux governs the observed variability. To directly understand the role of the magnetic field in energizing the solar corona, it is necessary to measure the free magnetic energy available in active regions. The grant now expiring has demonstrated a new and valuable technique for observing the magnetic free energy in active regions as a function of time.

The magnetic energy of an active region is derived from the magnetic virial theorem (e.g. Molodenskii, 1969; Aly, 1984; Low, 1984; Aly, 1989) which gives the total (force-free) magnetic energy as

$$E_{ff} = \frac{1}{4\pi} \int_{z=z_0} (xB_x + yB_y)B_z \, dxdy \ , \quad (1)$$

where B_x, B_y, and B_z are the horizontal and vertical components of the magnetic field, x and y are the horizontal coordinates on the Sun (e.g. Gary and Hagyard, 1990), and z_0 is the lower boundary. When assumptions that (a) the magnetic field is force-free, (b) that all the magnetic field crossing the chromospheric boundary is measured, and (c) that the coronal magnetic field falls to zero somewhere outside the active region are imposed, the virial theorem yields the total magnetic energy in the coronal volume threaded by the field lines crossing the lower boundary. If the lower boundary is measured at an atmospheric level where the magnetic field is force-free, then the magnetic virial theorem may be invoked to measure the total magnetic energy above active regions. Subtracting the energy of the equivalent potential field (with the same vertical field as that observed) from the total magnetic energy yields the free energy in the coronal volume, *i.e.*, the energy that is available to power solar activity.

At first glance it appears that the magnetic energy will depend on the coordinate system chosen, since equation (1) contains the coordinates x and y. However, if the magnetic field is force-free on the boundary, the horizontal Lorentz forces, given by

$$\begin{aligned} F_x &= \frac{1}{4\pi} \int_{z=z_0} B_x B_z \, dxdy \\ F_y &= \frac{1}{4\pi} \int_{z=z_0} B_y B_z \, dxdy \ , \end{aligned} \quad (2)$$

are zero. Hence, equation (1) is independent of the coordinate system and valid when the field is force-free.

Measurements of active-region photospheric vector magnetic fields have become routine. Quantities derived from the photospheric magnetic field have been used for years to characterize solar active regions and their propensity for solar activity. However, the measurement of the active-region photospheric vector magnetic field limits our physical understanding of the solar atmosphere in a fundamental way: the photosphere is still forced, *i.e.*, the plasma $\beta = P/8\pi B > 1$ and $\mathbf{J} \times \mathbf{B}$ can be non-negligible. Hence, the use of the *photospheric* measurement to understand the *coronal* magnetic structure is compromised to an uncertain degree.

A method for directly measuring the magnetic free energy in active regions was pioneered by Metcalf *et al.* (1995), based upon the *chromospheric* vector magnetic field derived from observations of the NaI D-line at

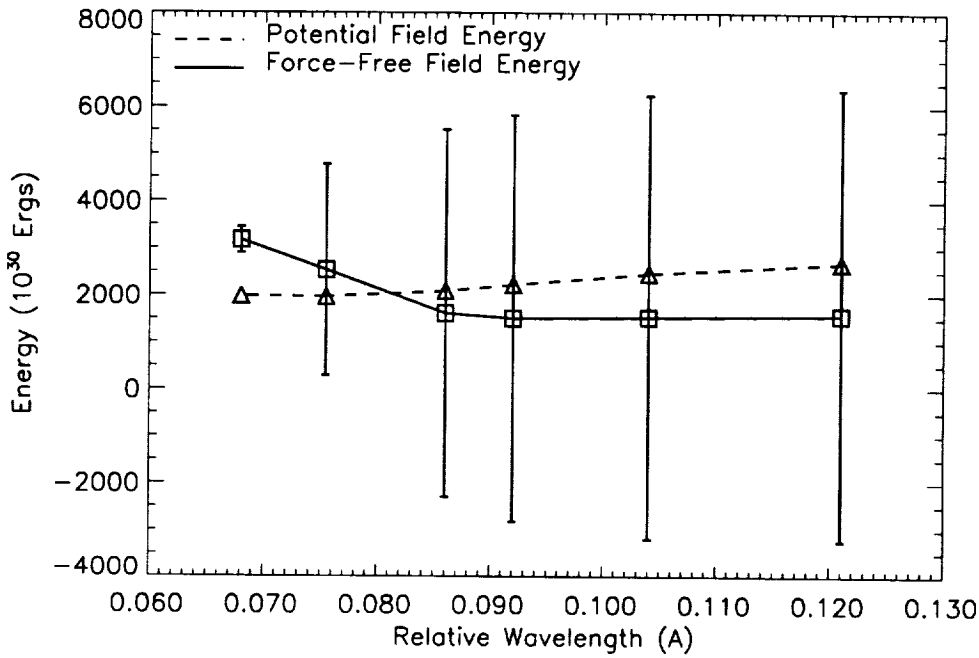

Figure 1: The magnetic free energy is measurable only with chromospheric data: only the data point highest in the atmosphere (closest to line center wavelength) samples the field in a *force-free* region. Here the virial theorem gives a valid measure of the magnetic energy in AR 7216.

5896 Å. This magnetically sensitive spectral line is formed high enough so that the magnetic field is force-free ($\mathbf{J} \times \mathbf{B} \approx 0$) but low enough so that the Zeeman polarization signals are sufficiently strong for a reliable measurement. In the initial Metcalf *et al.* (1995) study, the Stokes polarization spectra across the Na I line were recorded with the Haleakalā Stokes Polarimeter (HSP) at Mees Solar Observatory, Hawai'i as the instrument rastered across NOAA Active Region (AR) 7216.

Metcalf *et al.* (1995) determined the height at which the measured field becomes force-free. When the magnetic field is *not* force-free, Lorentz forces (Eq. 2) are non-negligible and the virial theorem breaks down. Figure 1 demonstrates this effect: magnetograms constructed from the polarization signal at wavelengths farther from line center (*i.e.*, deeper in the solar atmosphere) result in error bars that become exceedingly large and a computed total energy which is less than the energy of the equivalent potential field. This unphysical state is directly due to the breakdown of the assumptions listed above, *i.e.*, an indication that the atmosphere in these deeper layers is not force-free.

Hence, we must observe the magnetic field in the chromosphere, high enough above the photosphere so that the field is force-free, if we are to routinely apply the virial theorem. Figure 1 demonstrates that, below $\Delta\lambda \lesssim 80$mÅ from Na I line-center, the potential field energy drops below the total energy,

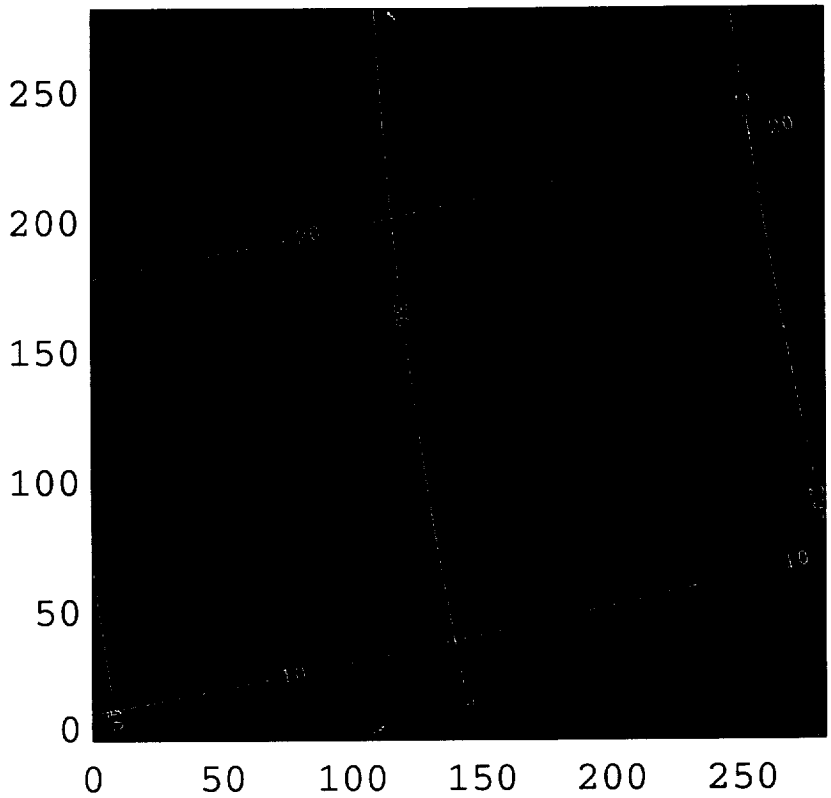

Figure 2: The IVM chromospheric line-of-sight magnetic field in AR 8299 overlaid on a continuum image. Red contours show fields directed towards the observer and blue contours show fields directed away from the observer (100, 200, 400, 800 G). Yellow contours show the latitude and CMD; the axes are labeled in arc seconds. The dark triangles and the apparently strong magnetic field which appear at the center of the extreme upper and lower edges are from fiducial marks in the IVM and are neither real nor included in our calculations.

and by $\Delta\lambda \approx 68$ mÅ the chromospheric magnetic field fulfills the force-free criterion and provides a reliable measure of the magnetic energy using the virial theorem.

2 Recent Advances

2.1 Multi-wavelength observations

Under this grant, the IVM and Mees Observatory conducted three separate campaigns to observe in the chromospheric Na-D line. Table 1 lists the dates of these campaigns and Figure 2 shows a single example from this dataset.

To advance the science goals of this grant, we undertook these campaigns to observe chromospheric magnetograms with the IVM in it's old configuration. From 7-Aug-1998 through 4-Sep-1998, a total of 29 active regions were surveyed and 17 movies sequences recorded. From 19-Dec-2000 through 1-Feb-2001, a total of 41 active regions were surveyed, and 12 movie sequences recorded.

Data from these campaigns is under active analysis.

The HI H-alpha line was observed during 26-Jul-2001 through 09-Aug-2001. This was a first attempt to make IVM magnetograms in the Hα line. Despite a number of setup problems, quick-look analysis shows that valid signal was detected in all Stokes parameters in many active regions. Analysis of these data will be conducted to assess the utility of H-alpha observations for characterizing the chromospheric field at a higher altitude than is seen in NaI-D.

2.2 IVM Hardware Modifications

2.2.1 Tunable filter development

The IVM air-gap Fabry-Perot etalon is a high quality spectrometer. With a finesse of 50, it is one of the best operational etalons in regular use for solar observations. Because it is designed to provide high spectral resolution FWHM of 70 mÅ, the free spectral range (the separation between etalon orders) is 3.5 Angstroms. Therefore, we need a blocking filter that has a FWHM of 3 Angstroms or less. Such narrow filters are available, but limit the range of spectral scans within a single line, reduce overall system transmission, and are sensitive to alignment and temperature variation. It was desirable therefore to develop a tunable blocker that could be used in conjunction with the etalon, and would permit rapid switching among widely separated spectral lines.

As originally designed, the IVM was to use an acousto-optic tunable filter. That technology did not mature, and we had to fall back to fixed interference filters as blockers. The time to open the system, remove the blocker, install a new one, close and stabilize the system is one day. Therefore, comparisons between photospheric and chromospheric magnetograms and/or structure images are not possible.

Under this grant, we pursued a new technology: liquid crystal tunable etalons. This technology was initially developed for use in aeronomy, both ground and space-based (Schneller et al., 1996) The potential advantages of these etalons are many:

- Wide angle of acceptance. The index of refraction of the liquid crystal is in the range 1.5 to 1.8, increasing the angle compared to a gap etalon.
- Rapidly tunable at low voltage.
- Stable alignment. Gap etalons regularly lose parallelism and must be realigned. Liquid crystal gaps are set by mechanical spacers.
- Low cost.
- Compact design. Gap etalons require significant structure around the clear aperture to hold the drivers and sensors for the tuning system.

The liquid crystal etalons are produced by Scientific Solutions, Inc. Initial discussions with the vendor demonstrated that many of the basic problems unique to our application were tractable. In aeronomy applications, overall transmission is critical, therefore reflector coatings are held to modest reflectance in order to minimize absorbance. Typical etalons then have a finesse of 15, reflector limited. The surface flatness and parallelism of the substrates appeared not to limit the finesse.

For the IVM, we decided to attempt to accomplish both rapid switching among lines

Dates	Spectral line	Comments	
03-Jul-1996 – 30-Jul-1996	NaI		
07-Aug-1998 – 04-Sep-1998	NaI	29 Active Regions	17 Movie sequences
19-Dec-2000 – 01-Feb-2001	NaI	41 Active Regions	12 Movie sequences
26-Jul-2001 – 09-Aug-2001	Hα		

Table 1: NaI Data were obtained in three separate observing campaigns.

The Magnetic Free Energy in Active Regions, Thomas R. Metcalf and Donald L. Mickey 1999), American Astronomical Society Meeting 194, 9407

A Comparison of the Active Region Magnetic Field in the Photosphere and Chromosphere., Thomas R. Metcalf and K. D. Leka 2001, American Geophysical Union, Spring Meeting 2001, abstract #SP41B-07 441B07

A Comparison of the Active Region Magnetic Field in the Photosphere and Chromosphere, Thomas R. Metcalf and K. D. Leka 2001, American Astronomical Society, Solar Physics Division Meeting

The Magnetic Free Energy and a CME in Active Region 8299, Thomas R. Metcalf, Donald L. Mickey, Barry J. LaBonte, and Leigh Ann Ryder, Astrophys. J., submitted, 2001.

Active Region Magnetic Structure Observed in the Photosphere and Chromosphere, K. D. Leka & Thomas R. Metcalf 2001, Astrophys. J., in preparation

Table 2: Publications acknowledging this grant.

and broader tuning within a spectral line. This requirement can be met with a pair of etalons, each having finesse 30. Models of the solar spectrum times the etalon transmission were computed by us and by the vendor as a check on our mutual understanding of the materials properties and the etalon performance. After many iterations, a design for a pair of etalons used in vernier mode was settled upon as optimal. This would permit scanning to any wavelength between 580 and 660 nm, with a parasitic light level of a few %, no more than the present IVM. By using the availability of standard spacers and offsetting the index of refraction of the liquid crystal, a wide choice of vernier ratios could be tried. The optimal design etalon pair had spacer thicknesses of 10 and 15 microns, and indices of 1.79 and 1.58 respectively, for a vernier ratio of 1:1.32.

The vendor worked out a design for a higher reflectance coating that would permit higher etalon finesse. The coating was deposited on a substrate, its reflectance verified, and the distortion of the substrate measured. The substrates for the etalons were then figured with a compensating distortion. When they were coated, they then are flat. Both the reflectance and surface figure appeared to meet the requirements.

The etalons were assembled and tested. One had a measured finesse of 18, and the other a finesse of 10. The overall transmittance was lower than expected. The cause of the finesse failure is not certain, but may be related to the two additional steps that occurred after the reflectors were tested: deposition of the transparent electrodes, and wip-

ing of the surface to align the liquid crystal molecules. The cause of the transmission failure is likely higher than expected absorbance in the coatings, an effect difficult to characterize by direct measurement.

After discussion of alternatives, it was decided that this technology is not yet capable of the higher requirements that the IVM application places upon it. It remains a technology of high potential, and new materials handling techniques, such as atomic-beam alignment of the LC molecules (Chaudhari et al., 2001) in place of mechanical rubbing may improve the performance for applications similar to the IVM.

2.2.2 Filter Wheel

The fall-back plan against a failure of the LC etalons was to install a filter wheel in the IVM Data Camera beam. The original IVM blocker filters were fabricated in the early 1990's; nearly a decade of progress in that technology made it possible to procure filters with higher transmission and steeper cutoff of offband light. However, limited space is available in the IVM instrument where the wheel must be located. To accommodate the wheel, a new sub-plate had to be fabricated.

The mechanical parts for the wheel are complete. The motor, drive, and filter thermal control components are procured. The IVM observing software was designed with the components for a tunable filter, which will be used to sequence the wheel with the observing program. We expect to have the wheel test run within a month, as the last elements are integrated. At a later time, we will change the final camera lens and add a lens adjacent to the wheel to render the beam telecentric, improving the uniformity of the blocker filters over the FOV.

2.3 Enhancement to the IVM Data Reduction Software

At the start of this grant, the IVM data reduction software was not capable of analyzing the NaI data. The first analysis task that faced us was to upgrade the IVM software to allow the analysis of the data listed in Table 1. The software was originally designed to work with the relatively narrow FeI lines and the broad NaI line required substantial modifications to the analysis software. The enhancement of the software is complete and the data reduction software is now capable of routine analysis of NaI data.

2.4 Observations of the 3-D Structure of Sunspots

Advances in the inversion procedures of Stokes spectra have enabled photospheric-line spectropolarimetry to reveal the depth-dependence of a number of quantities of interest. Westendorp Plaza et al. (2001a, 2001b) have demonstrated techniques which, when applied to the 630.15,.25nm Fe-I photospheric lines, result in depth-variation information of the vector magnetic field, temperature, and velocity stratification between $-2.5 < \log \tau_5 < 0$. This is roughly a vertical span of 300km from deep in the photosphere to just below the chromosphere. The results of this approach are promising but still limited to a narrow range of atmospheric heights. Additionally, these authors focus squarely on the variations observed in the penumbra of a small sunspot.

A first direct comparison of vector magnetic fields in the photosphere and chromosphere with near-cotemporal observations

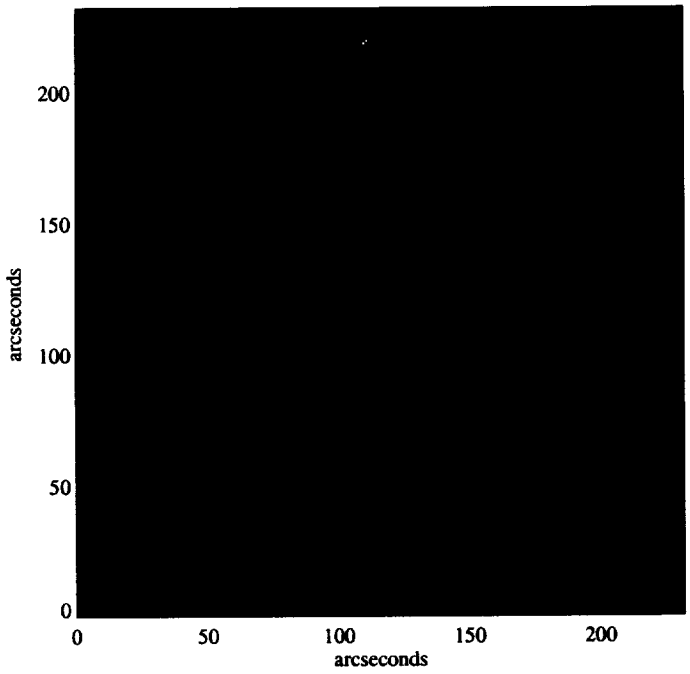

Figure 3: Continuum image of NOAA AR8299 from the Imaging Vector Magnetograph obtained near the Na-I 589.6nm line. Contours show the sunspots observed with the Advanced Stokes Polarimeter in the continuum near the Fe-I 630nm lines.

used ASP and IVM data from NOAA AR8299 (N19 W62) on 18 August 1998 (Fig. 3). The Advanced Stokes Polarimeter scanned this active region from 13:44–13:56UT in the photospheric Fe-I lines described above. Observations with the Imaging Vector Magnetograph scanning the chromospheric Na-D line began at 17:23 UT and continued for many hours with a 3–5 min. cadence. For the initial analysis, we increased the IVM signal-to-noise ratio by averaging the spatially-coaligned spectra of eleven datasets from 17:23–17:53, all of which had good seeing.

The preliminary comparison of these two datasets (to be submitted for publication in Autumn 2001) was work funded primarily by NASA through NASG-00031 and this grant. We present the main results here. First and foremost, a comparison of the magnetic flux observed at the two layers is shown in Figs. 4, 5 and 7.

The observed changes between the photospheric and chromospheric vector magnetograms include a weakening of the total magnetic flux at the higher layers (Figs. 5, 7). This is hardly surprising, but the magnitude of the weakening is. Note that the comparisons here are limited to quantities derived without performing the ambiguity-resolution of the transverse component of the magnetic flux. The reason for this limitation is that, for observations close to the limb, the ambiguity resolution (*e.g.*, Metcalf, 1994) requires mixing between the transverse and line-of-sight fields to derive the horizontal and vertical

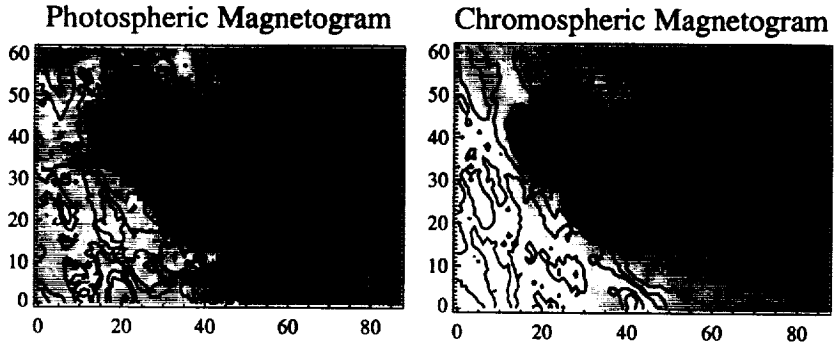

Figure 4: Magnetic Flux maps showing the line-of-sight (contours: —— = positive, at 50,100,200,400,800,1600G levels) and transverse (line-segments), magnetic flux components. Top: photosphere, binned to 1″ pixels, maximum B_t=2500G. Bottom: chromosphere, maximum B_t=1700G.

fields and the ambiguity resolution becomes less reliable. This is obviously a limitation of this dataset (and a strong motivation for additional coordinated observations).

Additionally, the direct comparison of the two datasets clearly shows the superpenumbral structure of the sunspots. Westendorp Plaza *et al.* (2001a) detected the sunspot canopy as an increase in the magnetic field strength with height (through the upper photosphere) beyond the visible penumbral boundary. We detect the magnetic canopy or superpenumbra directly in the chromosphere, as a positive fractional change in total flux (Fig. 7) occurring outside the photospheric penumbral boundary (Fig. 8).

2.4.1 Heights of Formation and Heights of Detection

At disk center, the Fe-I lines are formed over the range 250–350km above $\tau_{500\text{nm}} = 1$ (Bruls *et al.*, 1991), and, in the VAL-F model atmosphere, the Na-D line is formed at approximately z = 1000km above $\tau_{500\text{nm}} = 1$ at 68mÅ from line-center in the quiet sun (e.g. Metcalf *et al.*, 1995). Hence, from quiet Sun models at disk center, a first estimation of Δz, the difference in the height of formation of Fe-I and Na-D, is of order 700 km. A correction to this must be made for the observations presented here, in that the observing angle $\mu = 0.47$. Spectral features which form at optical depth unity form at $\tau_{\text{vert}} = 1/0.47$ when the atmosphere is viewed at an angle corresponding to $\mu = 0.47$. This is typically less than one density scale height higher than $\tau_{\text{vert}} = 1$ (assuming an exponentially stratified atmosphere). In a non-magnetic atmosphere this would be only 100 km. However in a sunspot's magnetic atmosphere the variation in Δz could be significantly greater.

To better grasp the Δz question we performed a simple test. The active region was

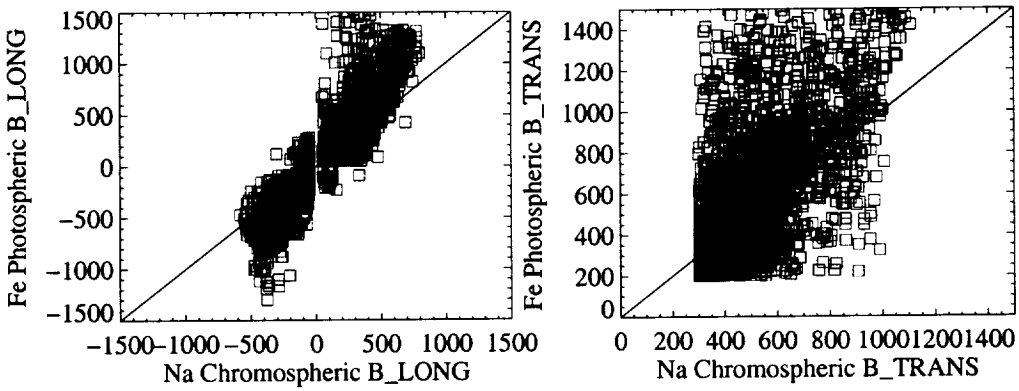

Figure 5: Comparison of the photospheric horizontal axis and chromospheric (vertical axis) line-of-sight (left) and transverse (right) magnetic flux. Error bars are omitted for clarity, however points below the noise levels are not plotted.

very close to a potential configuration, with a region-averaged twist parameter $\alpha_{rmAR} \approx -0.008$ Mm^{-}1. Extrapolations in height from the photospheric flux were performed, and compared to the observed chromospheric flux. The goal was to find the height at which they best agreed (Fig. 9). The results are surprising: the best agreement comes with a Δz =2–2.5Mm.

2.4.2 Magnetic scale heights

The logical extension from these initial results is to investigate dB/dz and the implied magnetic scale heights. Using the mean Δz derived from the quiet-sun models (0.7 Mm) and the extrapolations (2–2.5 Mm), and allowing for the possible range implied by their substantial difference, we show in Fig. 10 the inferred dB/dz across different sunspot components. We find values which are generally lower than the $\approx$ 2 G/km derived from deep-photosphere/upper-photosphere observations (Westendorp Plaza *et al.*2001a; Pahlke & Wiehr 1990) but which agree with previous observations of the photosphere/chromosphere values, generally $\approx 0.5 \pm 0.2$ G/km with lower values in the penumbral than umbral regions (Ruedi, Solanki, & Livingston 1995a; Ruedi *et al.* 1995b).

Inverting this quantity (dB/dz) and normalizing by the photospheric magnetic flux gives us the implied magnetic scale heights (Fig. 11). The most obvious feature in the scale height is the uniformity in the umbra, demonstrating that the umbra is a monolithic structure filled with magnetic field. Such uniformity is expected given the large magnetic fill-factor in the photosphere and the consistency of the field strengths across sunspot umbrae. The second feature in the implied scale heights is a dramatic change once the umbral/penumbral boundary is crossed, from almost a single value in the umbra to a wide range covering almost an order of magnitude in the penumbra and plage.

The puzzling result is that no matter what end of the range of possible Δz used, the scale height is far differ-

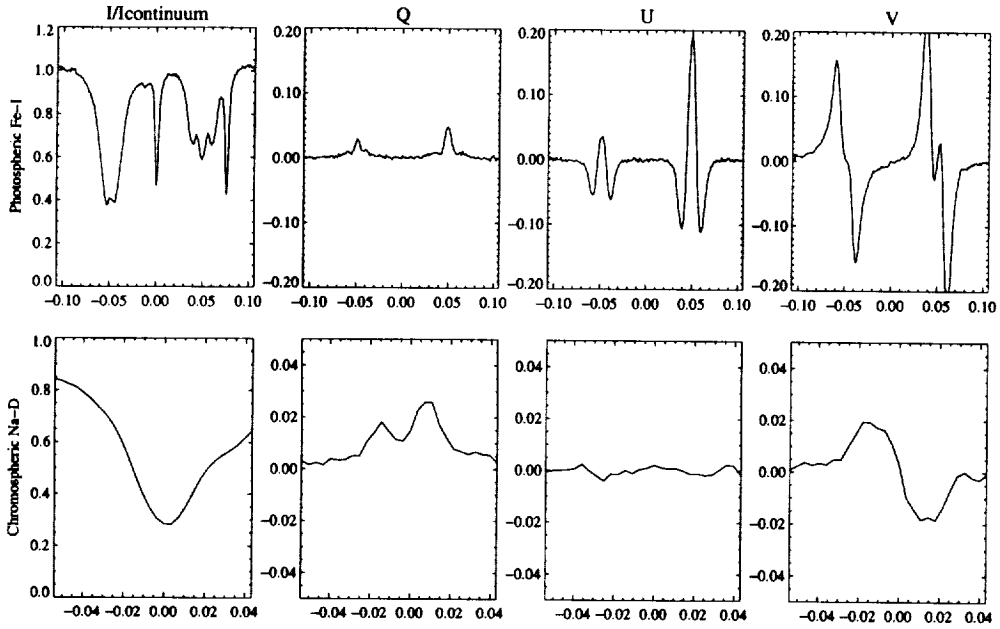

Figure 6: A comparison of photospheric and chromospheric Stokes profiles observed with the ASP and the IVM. The broad chromospheric NaI line is particularly well suited to a weak field analysis.

ent from what is expected. Generally the magnetic scale height, especially in the umbra, would be of the same order as the size-scale of the sunspot umbrae itself; in this case, at least 10Mm or 10^4 km. With a simple dipole model, the sunspot scale height increases linearly with height from a value roughly half the size of the umbra at the photosphere to a value consistent with the size of the umbra at a height which is also the same as the umbral diameter. Hence, there is a discrepancy of at least a factor of two between our results and the size of the sunspot itself (the sunspot magnetic field is decreasing with height more rapidly than expected), unless we neglect the atmospheric models and assume that the height we derive from the potential extrapolations is correct.

2.4.3 The Puzzle

The conundrum is simple: sunspot models which do not explicitly include magnetic fields indicate that chromospheric Na-D emission should come from a certain atmospheric height, while extrapolations from the photosphere lead to a much larger height.

The *modus operandi* until now has been to employ photospheric magnetic flux data as a boundary condition for coronal-field extrapolations. This approach explicitly ignores the transition from a plasma-dominated to magnetic-dominated regime ($\beta = P_{gas}/P_{mag} > 1 \rightarrow \beta < 1$). Preliminary evidence from our dataset points toward less of a discrepancy between coronal field extrapolations and coronal X-ray and EUV observations when chromospheric (force-free), rather than photospheric (non-

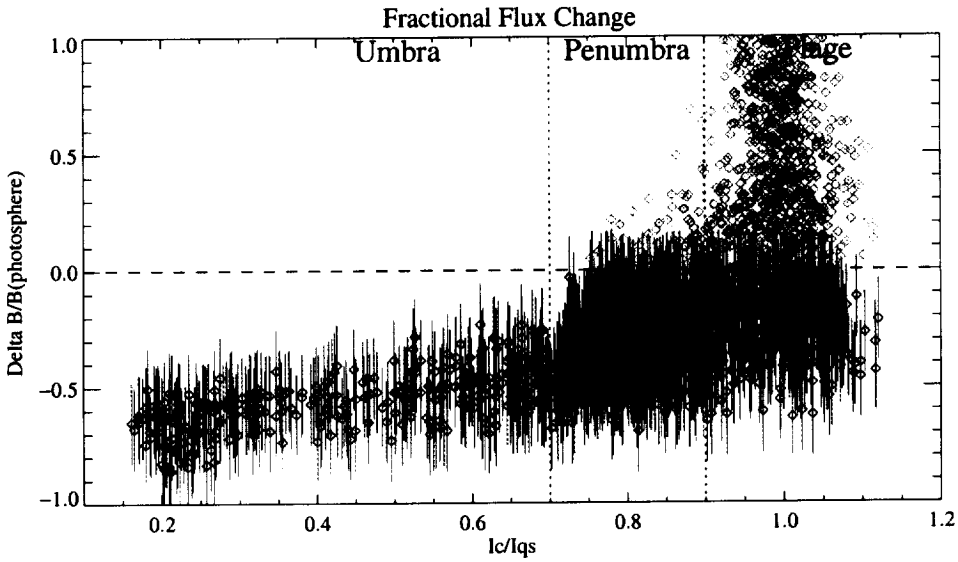

Figure 7: Percent change in total magnetic flux $B = \sqrt{B_l^2 + B_t^2}$ plotted as a function of continuum intensity (normalized by the quiet-sun mean intensity). The error bars reflect the uncertainties in both the photospheric and chromospheric flux measurements, and only points above the noise are considered. The (negative) fractional change in the umbra is a slight function of continuum intensity but consistent with a constant value. This is in contrast with the wide range of fractional change in the penumbra and plage. The points with positive fractional change, *i.e.*, with chromospheric flux greater than photospheric, occur only in the edge of the penumbra and in the plage regions, according to continuum intensity. As shown in Fig. 8, these points represent the direct detection of the superpenumbra, or canopy-like extension of magnetic field above and beyond the photospheric penumbra.

force-free), magnetic field measurements are used as boundary conditions for interpreting coronal (probably still force-free) conditions (Figure 12). Hence, the "problem child" is the photosphere/chromosphere transition.

Further, the interpretation of data from different atmospheric heights has routinely assumed single-values or single-ranges for the formation heights of a spectral line across very disparate solar structures. Observations are now forcing us to reconsider the simplistic assumptions and approaches of the past.

Sunspots are one building block of the solar magnetic cycle, exerting their influence over an enourmous atmospheric range. These bundles of strong magnetic fields influence solar accoustic signals below the photosphere and push aside extant magnetic structures into the corona. Active regions carry free magnetic energy which may power solar activity such as flares and Coronal Mass Ejections. The work funded by this grant has now forced us to confront some glaring inconsistencies in our understanding of basic sunspot structure.

2.5 Observations of the Magnetic Free Energy

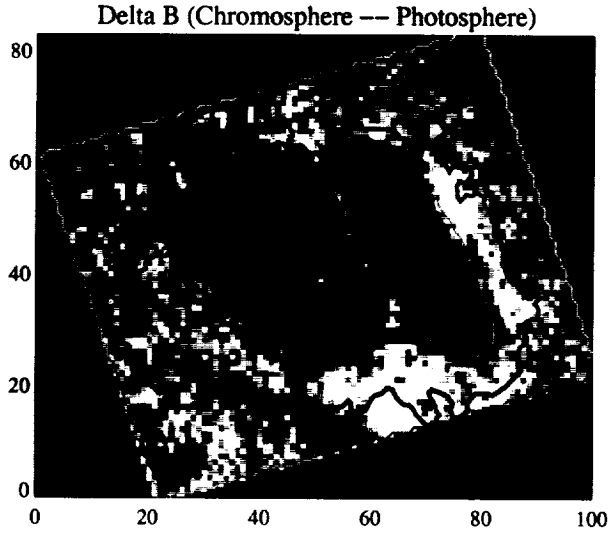

Figure 8: The super-penumbra as seen in a difference image between chromospheric and photospheric magnetic flux. Dark areas have negative fractional flux change (see Fig. 7), light areas have positive flux change and are highlighted by dark contour. Lighter contours indicate photospheric umbral and penumbral boundaries. Both the structure of the fractional flux variation and the location of the superpenumbra are visible in this example.

2.5.1 Confirmation of the Technique

Metcalf *et al.* (1995) measured the magnetic free energy with a single observation of a single active region, demonstrating the feasibility of this type of observation. While the technique successfully measured the free energy in AR 7216 at 10^{33} ergs (Figure 1), the vector magnetogram required nearly 5 hours of observations, making the HSP an impractical instrument for studying variations of the magnetic free energy.

With funds from this NASA grant, the U. Hawai'i/Mees Solar Imaging Vector Magnetograph ("IVM") was used to observe the chromospheric vector magnetic field in AR 8299 (Figure 2). The IVM (Mickey *et al.* 1996; LaBonte *et al.* 1999) has a symmetric design with near-normal reflections and a helium-filled telescope to minimize instrumental polarization and internal seeing. A four-frame polarization-modulation sequence is used; these mixed polarization states are sampled by means of a Fabry Perot etalon at 30 wavelength positions with 70mÅ FWHM spectral resolution across the magnetically sensitive line of choice; the default is the photospheric Fe I 6302.5Å line commonly used for photospheric vector magnetograms. By changing the prefilter, the IVM can obtain data in other spectral lines, including the Na I chromospheric line. The IVM was designed for active-region observations; it records spectropolarization images with 512×512 0.55″ pixels covering over $4' \times 4'$. A single spectrum-scan is obtained in under two minutes; to increase the signal/noise ratio, it

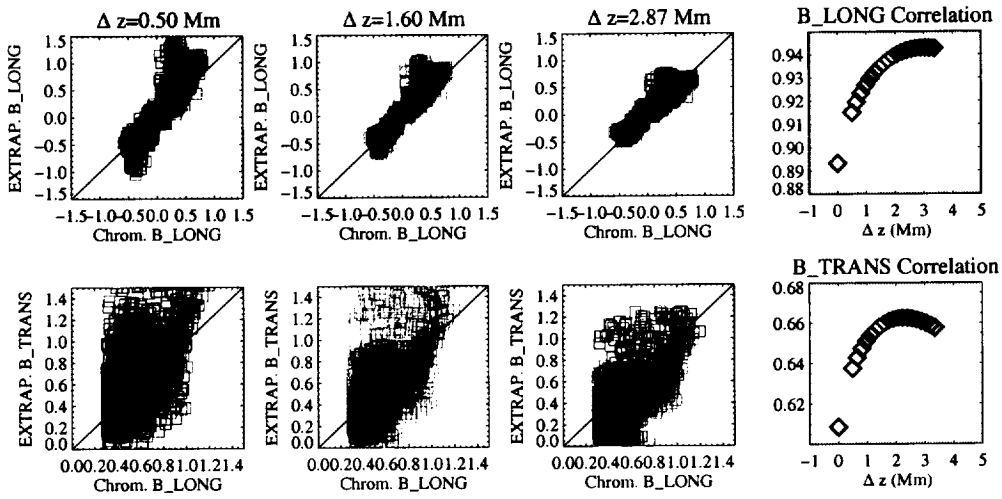

Figure 9: Comparison of the chromospheric (horizontal axis) B_long (left) and B_trans (right) magnetic flux to extrapolated flux (using the photospheric flux as the boundary). Bottom panels, the correlation coefficients for line-of-sight (left) and transverse (right) fluxes between the two, as a function of Δz between the two. Best fits, weighting the lower-noise higher-correlation B_l more than B_t, is Δz =2–2.5Mm. This contrasts with the expected $\approx$ 0.7Mm from non-magnetic stratified atmospheres (see text).

is common to average the spectra from two or more coaligned data sets before inversion to the magnetic flux vector.

On 1998 August 11, the IVM observed AR 8299 in the NaI spectral line for the Whole Sun Month campaign (Figures 2,13). From these chromospheric magnetograms, the total magnetic energy was computed as a function of time. The free energy is the total energy less the energy of the equivalent potential (current-free) magnetic field; the potential field energy, computed using the observed vertical field as a boundary condition (Fig. 14), was nearly constant at 10^{32} ergs.

The initial results confirmed the technique: first and foremost, the magnitude of the free energy in AR 8299 is consistent with the work of Metcalf et al. (1995) which used a very different instrument. The primary difference between this observation and the earlier work is the considerably smaller value of the potential magnetic energy found in AR 8299: the total energy is nearly an order of magnitude larger than the potential energy. The magnetic energy is about a factor of two lower than the open field limit given by Aly (1984), indicating that the large observed free energy is physically possible (dashed line in Figure 14).

The secondary difference is that the error bars for AR 8299 are somewhat larger than for AR 7216; this is due to some of the magnetic flux leaving the field-of-view and connecting to nearby AR 8297 (Figure 13). Recalculating the total energy for many different origins of the coordinate system will yield the same result unless the field is not force-free and/or significant flux is leaving the field-of-view. Any statistically significant variation of the energy with the coordinate

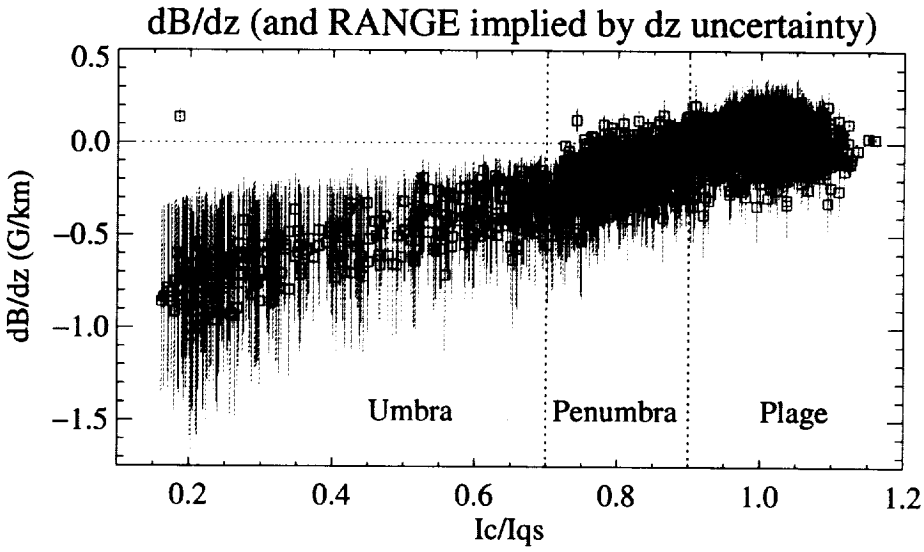

Figure 10: Inferred dB/dz from the photospheric and chromospheric total magnetic flux, as a function of Ic/Iqs. Points show the mean, "error bars" indicate the possible *range* of dB/dz given the possible range of formation heights for both the Fe and Na lines.

system will quantify these systematic effects. For AR 8299, the magnetograms are derived from $\Delta\lambda$=68mÅ from line-center where the field is believed to be force-free. Additionally, a careful analysis of the flux loss to AR8297 using KPNO data indicates that the flux loss is acceptable and the virial theorem applies.

2.5.2 Variation in the Magnetic Free Energy

As mentioned above, the IVM has the capability of obtaining a full vector magnetogram every few minutes, enabling not only the measurement of the magnetic free energy but also its *variation* in time: Figure 14 shows the total magnetic energy as a function of time for AR 8299. The free energy peaks at about $1.5 \pm 0.5 \times 10^{33}$ ergs, but drops to a level consistent with zero for almost an hour late in the observation before gradually increasing to the previous level. As the observation ended, the total magnetic energy approached the open field limit, suggesting that the field was in a substantially more open configuration compared to the field before the dip.

This intriguing observation will be discussed in some detail below since it is a good example of the type of observation that we have obtained with funds from this grant. The obvious question is, what led to this dramatic change in the magnetic free energy?

2.5.3 An Invisible CME?

The remarkable drop in the magnetic free energy observed between 20:30 and 21:30 UT was accompanied by almost insignificant soft X-ray activity on the Sun (Figure 15). There were no radio bursts reported during this time interval, the Mauna Loa coronagraph was not observing, and CGRO/BATSE saw no hard X-ray bursts. Unfortunately, no SOHO data are available and TRACE was

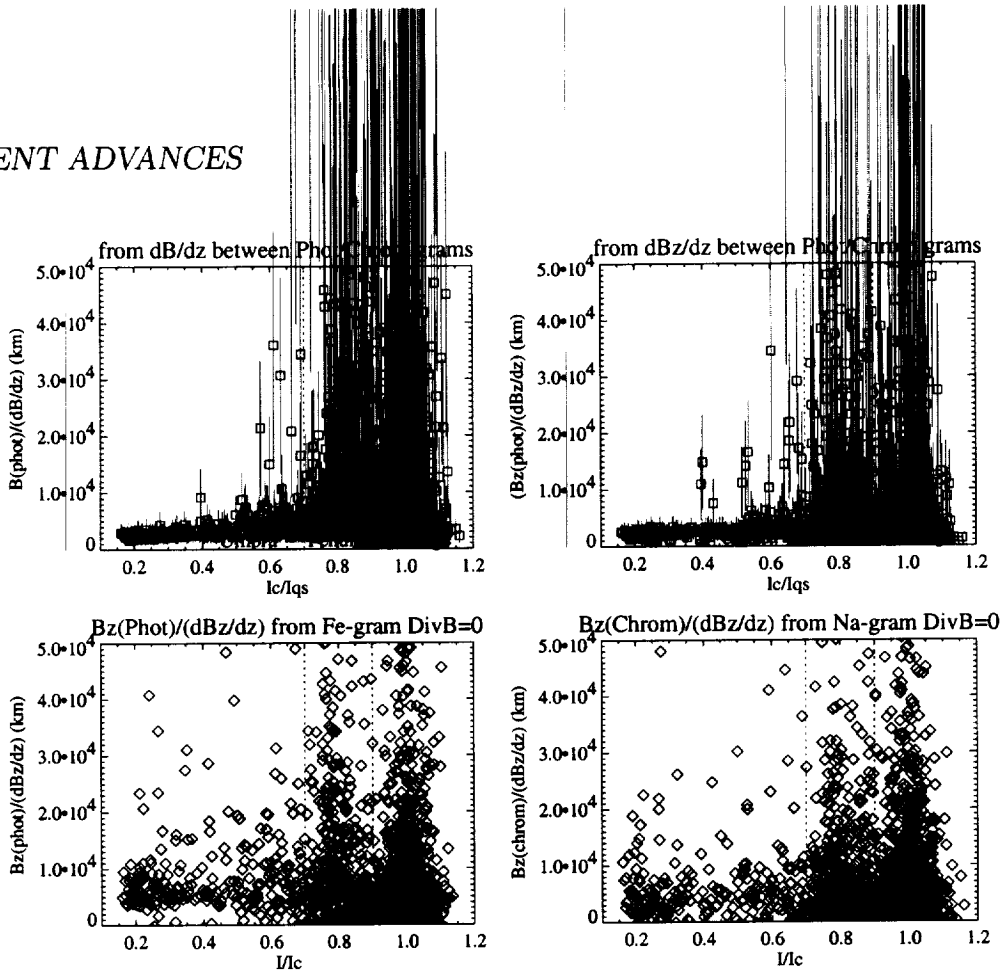

Figure 11: Similar to Fig. 10 but showing the implied magnetic scale height. The constancy of this scale height is remarkable over the umbra; the abrupt change in scale heights between umbra/penumbra is striking, although we use a constant *r*ange of Δz for all points regardless of their place in the sunspot.

not observing this active region. Hence, we have little information on what may have occurred in the corona of this active region during this time.

However, Figure 16 shows SXT composite images before and after the dip in the magnetic free energy (no SXT data are available for AR 8299 between 19:38 UT and 22:34 UT due to calibrations). There is a significant change in the X-ray structure of the active region at some time between the images in Figure 16 which includes the energy dip. The most obvious change is the appearance of a bright cusp connecting AR 8299 and AR 8297, seen in the center of the SXT ROI difference image. Unfortunately, we do not know exactly when this connection brightened. We also note that there was a faint soft X-ray sigmoid structure connecting AR 8299 with AR 8297 prior to the dip in the magnetic energy, though this structure does not appear to change between 19:38 and 22:34 UT.

The existence of an X-ray sigmoid, the development of a cusp structure, as well as the lack of a GOES event, are all signatures often associated with gradual, halo CMEs (e.g. Webb *et al.* 1998; Hudson *et al.* 1998; Canfield, Hudson & Pevtsov, 2000; Sheeley *et al.* 1999). Hence, the SXT data provide strong support for the occurrence of a

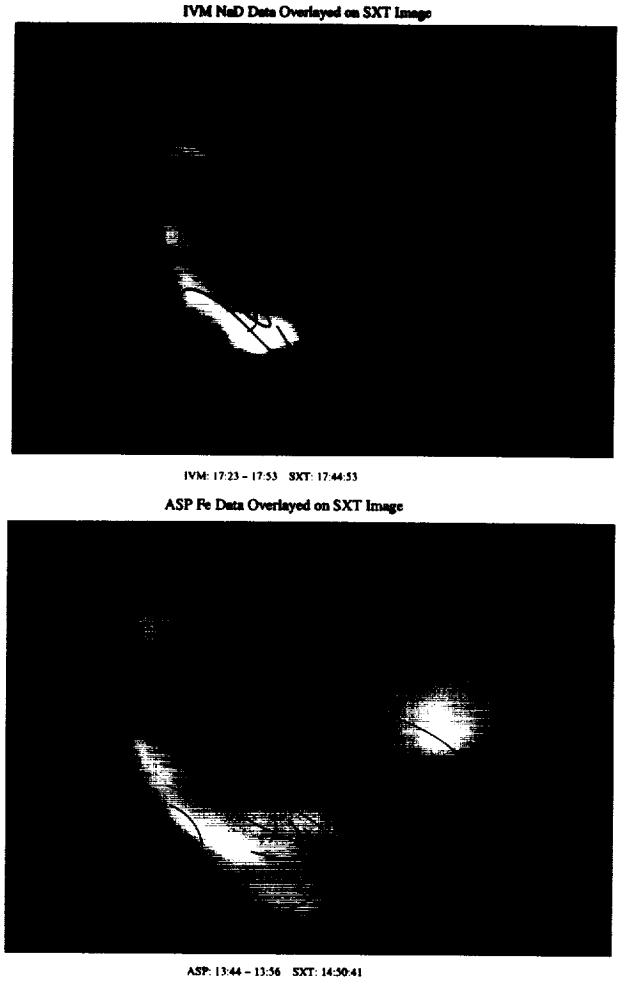

Figure 12: The magnetic field extrapolation from the chromosphere (top) matches the SXT data better than the extrapolations from the photosphere (bottom).

gradual CME. A CME without any remarkable effects in the low corona is not unheard of: Webb *et al.* (1998) report such an event from 1997 January 6, in which a geoeffective CME was associated with remarkably weak coronal activity (a GOES A1 event) and a combination of brightening and dimming in SXT images. This scenario is very reminiscent of the 11 August 1998 AR 8299 observation presented here. Without any data from SOHO/LASCO, we cannot be certain that such a CME occurred in AR 8299, however the circumstantial evidence suggests that a CME was launched.

The observation presented above is, to our knowledge, the first direct measurement of the time development of the magnetic free energy in an active region. Relating the observed changes in the free energy with activity on the Sun, we may have observed the direct energization of a gradual CME for the first time. The dramatic drop in free mag-

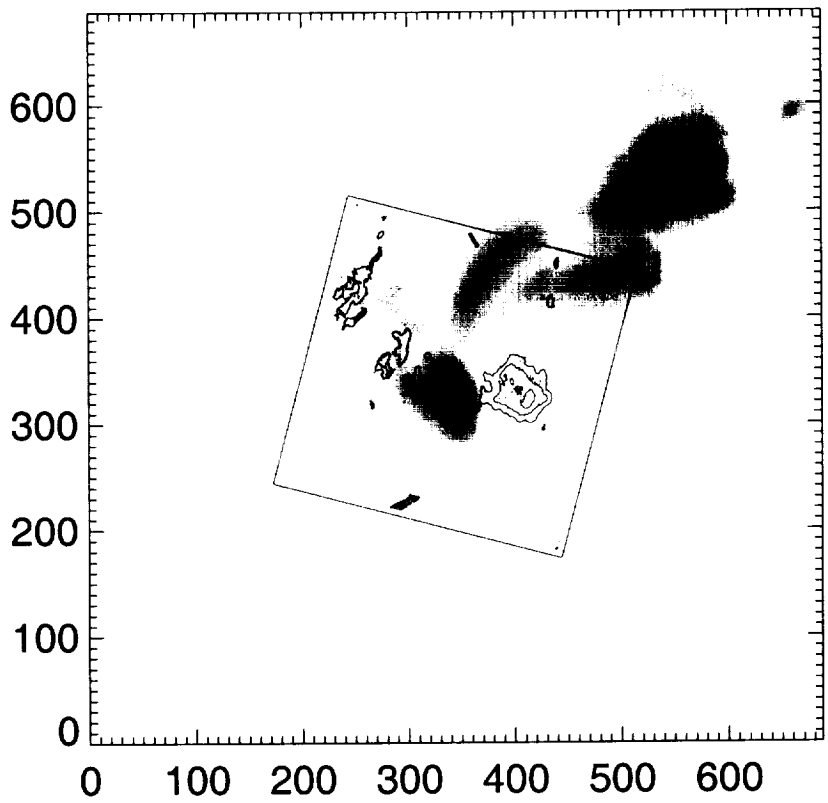

Figure 13: The line-of-sight magnetic field overlayed on an SXT image (negative image, logarithmically scaled). The gray square shows the IVM field-of-view. The magnetic field is the same as Figure 2 and the axes are labeled in arc seconds. AR8299 is in the center of the image and AR8297 is the upper right region.

netic energy observed in AR 8299 amounts to approximately 10^{33} ergs. This is in an enormous amount of energy given that there was no indication of flaring or other activity at the time of the energy dip. Where did the energy go?

While it is unlikely that a gradual CME could account for the full 10^{33} ergs (e.g. Antiochos *et al.* 1999), the topological change associated with a CME might redistribute the free energy out of the active region we observed. This hypothesis is supported by the rapid restoration of the free energy starting at 21:00 UT. The increase in free energy from 21:00 to 22:00 amounts to about 10^{33} ergs, implying a power input of 3×10^{29} ergs s^{-1}. While possible, it is unlikely that this energy build-up could come from photospheric motions over such a short timescale, since photospheric motions are typically only 1 km s^{-1} (e.g. equation (27) in Aly, 1989). Further, there is no observational evidence for emerging flux which might stress the coronal field more quickly. Hence, the redistribution of free energy within the AR 8299/8297 system, combined with a gradual CME, is a more likely explanation of the variation in the free magnetic energy. New observations which can be combined with Yohkoh/SXT and SOHO/LASCO data are required to fully

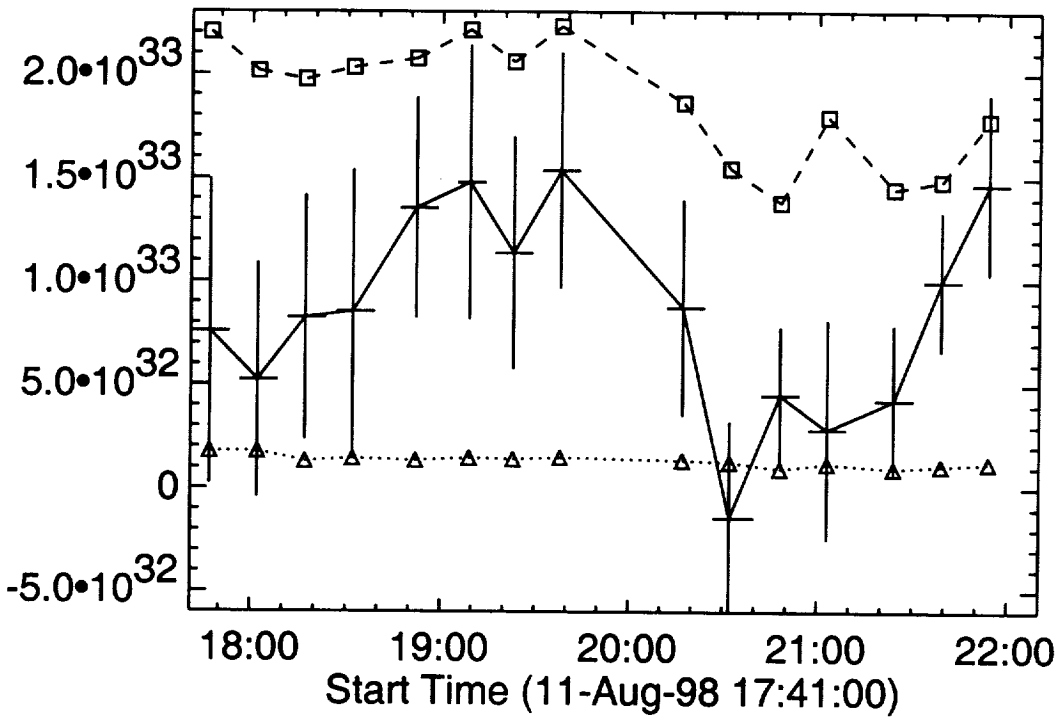

Figure 14: The total magnetic energy (ergs) above the chromosphere in AR 8299 (solid line) dips to a value consistent with zero around the time of a CME. The vertical error bars indicate both statistical and systematic errors. The horizontal error bars indicate the time interval over which each observation was averaged. The dotted line shows the energy of the equivalent potential field and the dashed line shows the equivalent open field energy.

understand the remarkable changes possible in solar active regions.

2.5.4 Where's the Flare?

The storage, loss, and subsequent gain of over 10^{33} ergs in this active region begs the question, why did it not produce a flare? There is sufficient free energy to power even a large solar flare, but energy storage alone is not a sufficient condition for the production of a flare. This observation verifies that, not only must energy be available in the magnetic field, but a proper field topology and a trigger must also be present. Apparently these conditions were not fulfilled in AR 8299. The precise conditions required for flares are not well understood and we expect further studies of the changes in magnetic free energy in flaring active regions to shed significant light on this subject.

While the dip in the free energy is the most remarkable feature of this dataset, the quasi-steady free energy outside this interval is also interesting. The magnetic energy stored in the active region magnetic fields is more than sufficient to explain the enhanced heating of the active region corona. In fact,

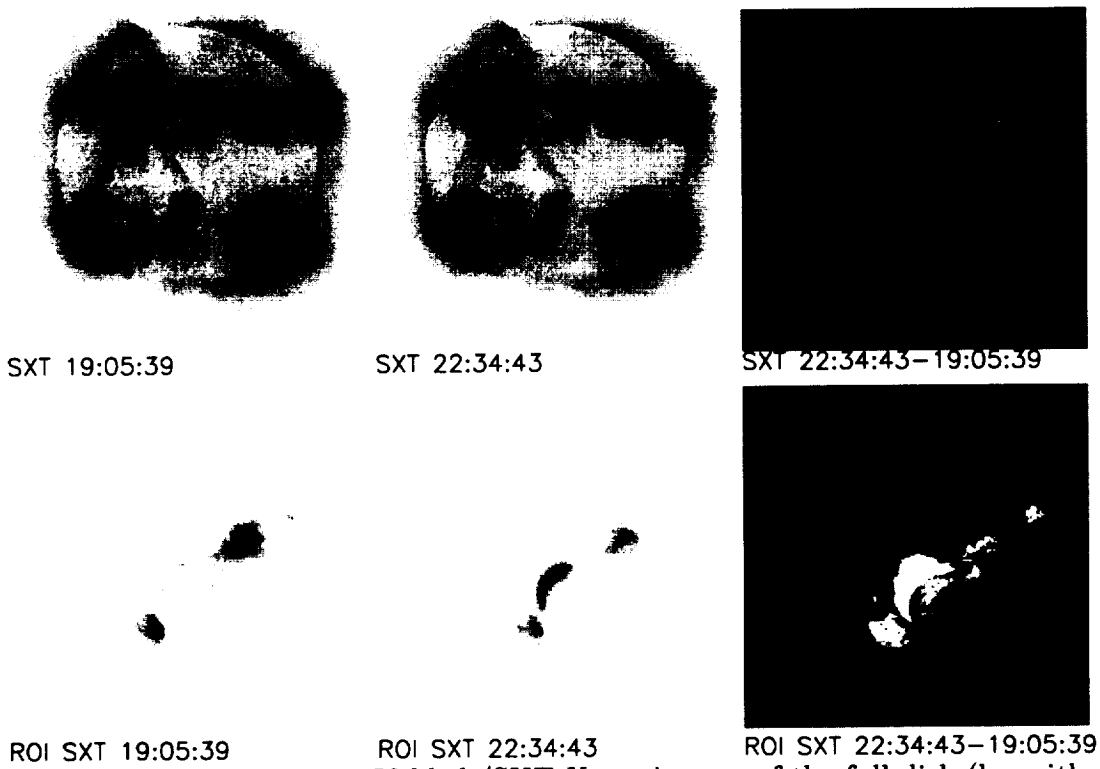

Figure 16: Composite, negative Yohkoh/SXT X-ray images of the full disk (logarithmically scaled) and AR 8299/8297 (linearly scaled) using the AlMg analysis filter. Left: before the energy dip. Middle: after the energy dip; Right: difference image. Around the time of the energy dip, a connection between AR 8299 and 8297 brightened dramatically.

dramatic change in magnetic free energy was accompanied by SXT observations suggestive of a gradual CME but the data are circumstantial. If a CME did occur in association with the drop in magnetic free energy, this would constitute the first direct evidence that the CME is powered by free energy stored in the magnetic field. New observations using the NaI D-line in conjunction with directed, coordinated space-based observations from Yohkoh, TRACE, SOHO, and HESSI are clearly called for at this time.

Our next goal will be to determine the physical changes which cause variations in the magnetic free energy. That is, we have seen the *effect*, but what was the *cause*? Ultimately, we hope to make advance predictions of solar activity by observing variations in the available magnetic energy. For a CME with little or no signature in X-rays, such as the event postulated here or the 1997 January 6 event studied by Webb *et al.* (1998), a dramatic change in the free energy may be the only indication, apart from coronagraph data, that a CME occurred.

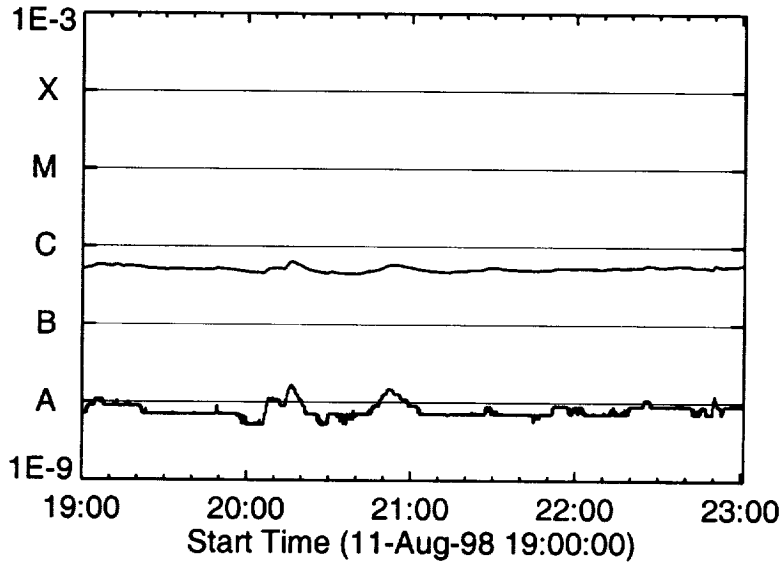

Figure 15: The GOES-10 soft X-ray light curves (W m^{-2}; upper curve: 1-8Å, lower curve: 0.5-4Å). There was no significant flaring activity in AR 8299 at the time of the CME and the dip in the magnetic free energy.

the 10^{33} ergs of free energy could power the observed X-ray emission (10^{26} ergs s^{-1}) for several months, even if it were not replenished, and it is much larger than a simple estimate of the thermal energy ($< 10^{29}$ ergs) in the active region corona. It has been suggested that the energetics of the quasi-steady enhancement of the heating in the active region corona is dominated by the magnetic field (Fisher *et al.* 1998). In the case of AR 8299 we have found that the free energy is more than sufficient, by several orders of magnitude, to counter the X-ray radiative energy losses in the active region and to explain the enhanced heating of the active region if the magnetic energy can be converted to thermal energy.

3 Conclusion and Future Work

Since the magnetic field in coronal active regions very likely dominates the energetics of coronal activity, measurement of the magnetic free energy available to the corona is an important step forward in our understanding of active regions. With the support of this grant, we have now demonstrated the feasibility of making temporally resolved measurements of the magnetic free energy above active regions. We have shown that the chromospheric magnetic flux vector, measured high enough above the photosphere so that the magnetic field is force-free, renders the magnetic virial theorem applicable.

We are now in a position to fully exploit this new tool. The observations presented herein demonstrate the usefulness of the technique, however, the results provide a mystery: where did the free energy go? A

4 References

Aly, J. J. 1984, Astrophys. J., 283, 349
Aly, J. J. 1989, Solar Phys., 120, 19
Antiochos, S. K., DeVore, C. R., & Klimchuk, J. A. 1999, Astrophys. J., 510, 485
Bruls, J. Lites, B. W., & Murphy, G. A. 1991, in Solar Polarimetry, Vol. 11 of NSO/Sacramento Peak Summer Workshop series, p. 444
Canfield, R. C., Hudson, H. S., & Pevtsov, A. A. 2000, IEEE Transactions on Plasma Science 28, 1786.
Chaudhari, P. and 26 coauthors: 2001, Nature, 411, 56. "Atomic-beam alignment of inorganic materials for liquid-crystal displays"
Fisher, G. H., Longcope D. W, Metcalf, T. R., & Pevtsov, A. 1998, Astrophys. J., 508, 885
Gary, G. A., & Hagyard, M. J. 1990, Solar Phys., 126, 21
Hudson, H. S., Lemen, J. R., St. Cyr, O. C., Sterling, A. C, & Webb, D. F. 1998, Geophys. Res. Lett., 25, 2481
Jefferies, J. T., Lites, B. W., & Skumanich, A. 1989, Astrophys. J., 343, 920
Khan, J. I, & Hudson, H. S. 2000, Geophys. Res. Lett., 27, 1083
LaBonte, B. L., Mickey, D. L. & Leka, K. D. 1999, Solar Phys., 189, 1
Leka, K. D. & Skumanich, A. 1999, Solar Phys. 188, 3
Low, B. C. 1984, in Measurements of Solar Vector Magnetic Fields, ed. M. J. Hagyard (NASA CP 2374), 49
Metcalf, T. R., Jiao, L., McClymont, A. N., & Canfield, R. C. 1995, Astrophys. J., 439, 474
Metcalf, T. R. 1994, Solar Phys., 155, 235
Molodenskii, M. M. 1969, Soviet Astron.–AJ, 12, 585
Mickey, D. L., Canfield, R. C., LaBonte, B. J., Leka, K. D., Waterson, M. F., & Weber, H. M. 1996, Solar Phys., 168, 229
Pahlke, K. D., & Wiehr, E. 1990, Astron. Astrophys., 228, 246
Ruedi, I., Solanki, S. K., & Livingston, W. C. 1995a, Aston. Astrophys., 293, 252
Ruedi, I., Solanki, S. K., Livingston, W. C., & Harvey, J. 1995b, Aston. Astrophys. Supp. Ser., 113, 91
Schneller, K., Noto, J., Schneller, W. J., Kerr, R. B., Doe, R. A. 1996, American Geophysical Union, Fall Meeting 1996, SA32B-03 "A Novel, Liquid Crystal Fabry-Perot Spectrometer for Ground and Space Based Atmospheric Remote Sensing"
Sheeley, N. R., Walters, J. H., Wang, Y.-M. & Howard, R. A, J. 1999, Geophys. Res., 104, 24739
Sterling, A. C., Hudson, H. S., Thompson, B. J., & Zarro, D. M. 2000, Astrophys. J., 532, 628
Sturrock, P. A, Weber, M., Wheatland, M. S., & Wolfson, R. 2001, Astrophys. J., 548, 492
Tsuneta, S., Acton, L., Bruner, M., Lemen, J., Brown, W., Caravalho, R., Catura, R., Freeland, S., Jurcevich, B., Morrison, M., Ogawara, Y., Hirayama, T., & Owens, J. 1991, Solar Phys., 136, 37
Webb, D. F., Cliver, E. W., Gopalswamy, N., Hudson. H. S., & St. Cyr, O. C. 1998, Geophys. Res. Lett., 25, 2469

Westendorp Plaza, C., del Toro Iniesta, J. C., Ruiz Cobo, B., & Martinez Pillet, V. 2001b, Astrophys. J., 547, 1148

Westendorp Plaza, C., del Toro Iniesta, J. C., Ruiz Cobo, B., Martinez Pillet, V., Lites, B. W., & Skumanich, A. 2001a, Astrophys. J., 547, 1130